OPEN ACCESS

University of BRISTOL

Igonin, N., Verdon, J. P., Kendall, J. M., & Eaton, D. W. (2021). Large-Scale Fracture Systems Are Permeable Pathways for Fault Activation During Hydraulic Fracturing. *Journal of Geophysical Research: Solid Earth*, *126*(3), [e2020JB020311]. https://doi.org/10.1029/2020JB020311

Peer reviewed version

License (if available):
Unspecified

Link to published version (if available):
10.1029/2020JB020311

Link to publication record in Explore Bristol Research
PDF-document

This is the accepted author manuscript (AAM). The final published version (version of record) is available online via Wiley at 10.1029/2020JB020311. Please refer to any applicable terms of use of the publisher.

University of Bristol - Explore Bristol Research
General rights

This document is made available in accordance with publisher policies. Please cite only the published version using the reference above. Full terms of use are available:
http://www.bristol.ac.uk/red/research-policy/pure/user-guides/ebr-terms/

Large-scale fracture systems are permeable pathways for fault activation during hydraulic fracturing

Nadine Igonin[1*], James P. Verdon[2], J-Michael Kendall[3], David W. Eaton[1]

1. Department of Geoscience, University of Calgary, Calgary, Alberta, Canada.

2. School of Earth Sciences, University of Bristol, Wills Memorial Building, Queen's Road, Bristol, UK.

3. Department of Earth Sciences, University of Oxford, South Parks Road,

Oxford, UK.

* Corresponding Author. Email: naigonin@ucalgary.ca, Tel: +1 403 542 7053.

ABSTRACT

Induced seismicity due to fluid injection, including hydraulic fracturing, is an increasingly common phenomenon worldwide; yet, the mechanisms by which hydraulic fracturing causes fault activation remain unclear. Here we show that pre-existing fracture networks are instrumental in transferring fluid pressures to larger faults on which dynamic rupture occurs. Studies of hydraulic fracturing-induced seismicity in North America have primarily used observations from regional seismograph networks at distances of 10s of km, and as such lack the resolution to answer some of the key questions about triggering mechanisms. A high-quality dataset acquired at a hydraulic fracturing site in Alberta, Canada that experienced events over M_W 3.0 is presented for the purpose of analysing detailed mechanisms of fault activation. The distribution of event hypocentres, coupled with measurements of seismic anisotropy, reveal the presence of pre-existing fracture corridors that allowed communication of fluid-pressure perturbations to larger faults, over distances of > 1 km or more. The presence of pre-existing permeable fracture networks can significantly expand the volume of rock affected by the pore pressure increase, thereby increasing the probability of induced seismicity. This study demonstrates the importance of understanding the connectivity of pre-existing natural fractures for assessing potential seismic hazards associated with hydraulic fracturing of shale formations, and offers a detailed case exposition of induced seismicity due to hydraulic fracturing.

Significance statement:

Felt earthquakes have been observed in North America, Asia and the U.K. during, or shortly after, hydraulic fracturing for shale gas development. An increase in fluid-pressure is widely regarded as the primary mechanism for fault activation, but current models do not adequately explain time delays (hours-to-days) and activation distance (up to > 1 km) from the injection. Using high-resolution data acquired in close proximity to hydraulic-fracturing operations, we show that pre-existing natural fracture systems can provide permeable conduits for diffusion of fluid pressure to a fault of sufficient size to host a felt earthquake. Our model explains both the observed time delay and activation distance and implies that mapping fracture networks may play an important role in risk analysis for induced seismicity.

1. INTRODUCTION

The association of induced seismicity with hydraulic fracturing (HF) operations for shale gas extraction is well-established (e.g., Atkinson et al., 2016; Bao and Eaton, 2016; Clarke et al., 2019). The potential socio-economic impact of hydraulic fracturing-induced seismicity worldwide can be high (Atkinson et al., 2020), as exemplified by a M_W 5.3 event in China in 2018, which resulted in fatalities and billions of dollars in damages (Lei et al., 2019). Kao et al. (2018) identified at least 5 instances in western Canada of M > 4.0 induced events, while other notable cases of hydraulic fracturing-induced seismicity have been documented in Ohio (Friberg et al., 2014; Skoumal et al., 2015), Oklahoma (Holland, 2013) and the UK (Clarke et al., 2019). For many published case studies in North America, seismicity is recorded using regional seismograph networks at distances of 10s of km (or more), or local monitoring is installed after-the-fact once seismicity has started (e.g., Clarke et al., 2014; Darold et al., 2014; Friberg et al., 2014; Schultz et al., 2015a,b; Skoumal et al., 2015; Wang et al., 2016). With such limitations, further investigation into the causative mechanisms of induced seismicity is often hindered, meaning that competing hypotheses cannot always be conclusively tested (e.g., Deng et al., 2016; Schultz et al., 2017).

Debate persists about the relative contributions of pore-pressure increase or stress transfer in generating induced seismicity, including trade-offs that likely exist between these different mechanisms. For example, questions persist regarding the relative importance at various distances of pore pressure changes or stress perturbations (Segall and Lu, 2015; Goebel et al., 2017), as well as the magnitude of perturbation necessary to trigger induced seismicity (e.g., Westwood et al., 2017; Wilson et al., 2018; Hosseini & Eaton, 2018). Achieving a better understanding of causative mechanisms will have significant implications for strategies used to mitigate induced seismicity. Where regulations pertaining to induced seismicity have been implemented, they are typically tailored toward reacting to cases of induced seismicity rather than prevention or mitigation (e.g., Shipman et al., 2018; Kendall et al., 2019). An improved understanding of the causes of induced seismicity could improve pre-injection characterization of site-specific seismic hazards, enabling a better understanding of effective mitigation options at sites where induced seismicity could occur.

Here we use data from the Tony Creek dual Microseismic Experiment (ToC2ME), an academic field experiment in Alberta, Canada wherein hydraulic fracturing-induced seismicity was monitored using a purpose-built seismic network (Eaton et al., 2018). The largest events reached a magnitude of M_W 3.2, and over 25,000 events were detected. Using this high-quality dataset, we undertake a detailed investigation of causative mechanisms for fault activation during hydraulic fracturing.

1.1. Potential Mechanisms for Fault Reactivation during Hydraulic Fracturing

Fault reactivation by subsurface human activities is usually characterized in terms of Mohr-Coulomb effects. The *in situ* stress field acting on a fault can be resolved into normal (σ_n) and shear (τ) stresses. Fault activation is expected if the effective shear stress exceeds the Mohr-Coulomb envelope, given by

$$\tau > \phi(\sigma_n - P) + C, \quad (1)$$

where P is the pore pressure, ϕ is the friction coefficient and C is the cohesion. This relationship is often formulated in terms of Coulomb Failure Stress (*CFS*)

$$CFS = \tau - \phi(\sigma_n - P), \quad (2)$$

where a positive change in *CFS* implies that the stress conditions are perturbed toward failure, and a negative change implies that the stress conditions are moving toward greater stability. The Mohr-Coulomb threshold may be reached in one of three ways (or a combination thereof): 1) an increase in the effective shear stress; 2) a decrease in the normal stress; 3) an increase in the pore pressure.

Figure 1 depicts some of the mechanisms by which fault reactivation may occur during hydraulic fracturing. An increase in pore pressure is a widely recognized causative mechanism for fault reactivation, since hydraulic fracturing, by definition, entails the injection of pressurized fluids into the subsurface. However, shale rocks have exceptionally low matrix permeability, meaning that fluid leakoff and/or diffusion will occur at exceedingly slow rates compared with large-volume injection into a permeable formation (e.g., Atkinson et al., 2016). In most such cases, pore pressures sufficient to activate faults and fractures are expected to be confined to a region no larger than a few hundred meters from the injection point (e.g., Shapiro and Dinske, 2009).

Observations of fault reactivation occurring at larger distances has led some authors to invoke stress transfer via poroelastic coupling as an alternative mechanism for fault reactivation (e.g., Deng et al., 2016; Westwood et al., 2017; Goebel et al., 2017). The stress change from pore-pressure into the solid matrix, or the deformation associated with tensile fracture opening and shear-slip on pre-existing fractures, will affect the stress field in the surrounding rocks and increase CFS. If the host medium has low permeability, then stress transfer through the rock frame might be expected to act over larger distances than the pressure pulse associated with injection (e.g., Deng et al., 2016). Kettlety et al. (2020) have demonstrated for the Preston New

Road site in the UK a strong correlation between the locations of induced events, and areas that receive positive CFS changes produced by the tensile opening of hydraulic fractures. Alternatively, Eyre et al. (2019a) show that aseismic (slow) slip along faults can also trigger events at larger distances from a well.

However, the occurrence of seismicity at larger distances from a well does not preclude pore pressure increase as a causative mechanism, since pre-existing fracture corridors within the shale may create highly permeable pathways, extending the region of influence of elevated pore pressures along these pathways. This mechanism has been proposed for several HF-induced case studies (e.g., Holland, 2013; Schultz et al., 2015a; Westaway, 2017).

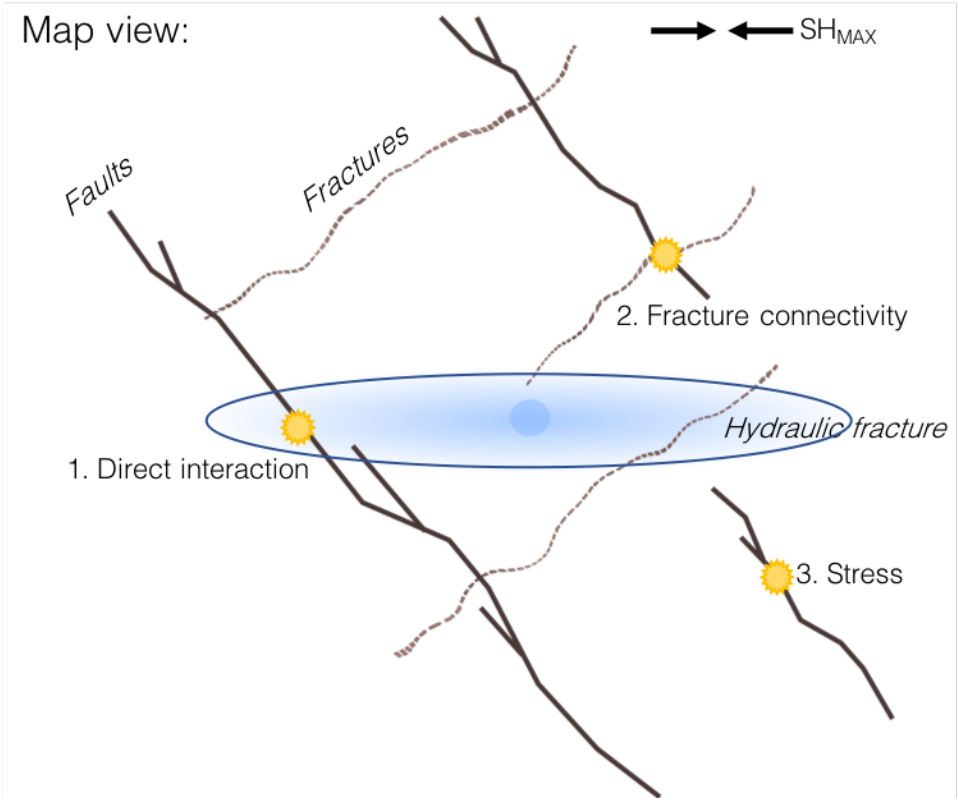

Figure 1: Various mechanisms by which hydraulic fracturing may cause fault reactivation: 1) hydraulic fractures (shaded blue region) may directly intersect a fault (e.g. Maxwell et al., 2010), 2) pre-existing permeable fracture corridors may transmit elevated pore pressures to a fault, and 3) stress transfer through the rock frame may increase the CFS acting on a fault.

In the following sections we introduce the ToC2ME dataset and examine the processes that occurred as faults were activated, timings and focal mechanisms of microseismic events. After discussing the stress field and interpreting trends associated with earthquake shear wave splitting, we combine these observations with fluid flow and geomechanical modelling, in order

to understand which of the above mechanisms are most consistent with the timing of fault reactivation.

2. DATA AND METHODS

The Tony Creek dual Microseismic Experiment (ToC2ME) is a research-focused field program acquired by the University of Calgary, using a suite of geophysical sensors to monitor hydraulic fracturing for shale gas in the Fox Creek area, northwest of Edmonton (Eaton et al., 2018). The monitoring array consisted of 68 shallow borehole stations, with each station comprised of vertical-component 10 Hz geophones cemented at depths of 12, 17 and 22 m and a 3-component 10 Hz geophone at 27 m. Additionally, 6 co-located broadband seismometers and 1 accelerometer were installed at the surface. The average station separation is 500 m with full azimuthal coverage in the region of the wells. Further details about the ToC2ME dataset can be found in a series of publications (Eaton et al., 2018; Igonin et al., 2018; Zhang et al., 2019; Poulin et al., 2019, Rodriquez & Eaton, 2020).

The site consisted of 4 horizontal wells drilled into the late Devonian Duvernay Formation at a total vertical depth of approximately 3,400 m. The Duvernay Formation comprises of a fine-grained organic-rich mudstone interfingered with carbonate (Knapp et al., 2017). It is overlain by the Ireton Formation, which consists of ~300 m of shale with low organic content, and it is underlain by the Beaverhill Lake Group, which consists of variability dolomitized carbonate platform and reef deposits (Knapp et al., 2017). The crystalline Precambrian basement occurs at a depth below surface of approximately 4000 m.

The Fox Creek area has experienced several nearby $M_W \geq 4$ events (e.g., Schultz et al., 2017; Eyre et al., 2019b) that have been attributed to hydraulic fracturing. Dozens of hydraulic fracturing pads can be linked to earthquakes between M_W 1 and 4 between 2013 and 2019 recorded by regional broadband seismometer networks (Schultz et al., 2019). Previously proposed explanations of the induced seismicity in this region relate to the presence of regional-scale N/S trending basement faults (Ekpo, 2020). Although there is limited known natural seismicity in this region, it has been suggested that natural earthquakes can be distinguished from induced earthquakes based on focal depth, since natural earthquakes in this region tend to occur between 5-20 km deep while induced seismicity generally occurs in the upper 4 km (Zhang et al., 2016).

The wells in this dataset were stimulated over a 4-week period in October – November 2016. Well C (see Figure 2) was stimulated first, from north to south along the well, after which the remaining wells were stimulated concurrently. In this study, we focus on the events that

occurred during stimulation of Well C. We do this because investigating and understanding the causes of fault reactivation is simpler early in the operation, during the initial stages of fault activation. After faults have initially been reactivated, causative processes become more ambiguous, since it may not be possible to distinguish processes that are directly linked to subsequent HF stages from aftershock sequences that persist due to inter-event triggering (e.g., Magshoudi et al, 2018) without any further anthropogenic contribution.

2.1. Event Detection and Hypocenter Location

The initial data acquisition and processing is described in detail by Eaton et al. (2018), and briefly reviewed here. Event detection was performed using an amplitude-based triggering algorithm to identify a set of template events. A matched-filter approach (e.g., Caffagni et al., 2016) was then used to detect smaller events with waveforms similar to the templates. A relatively low detection threshold was used, with the emphasis being avoidance of missed detections. After manual quality control to remove false positives, this produced a catalogue of over 25,000 putative events. Eaton et al. (2018) used a relative location method to compute event hypocentres, but low signal-to-noise ratios meant that only 4,083 events could be robustly located. The benefit of using this method is that the relative locations were able to highlight the key features in high resolution, with uncertainties of less than 50 m in map view and less than 100 m in depth view (Igonin et al., 2018).

All of the events located with the relative location method were above magnitude –0.5 and, as such, failed to capture events typically associated with hydraulic fracturing, which have a typical magnitude range of –3 to –0.5 (Eaton, 2018). To improve the magnitude of completeness and gain a better understanding of the event sequences, we used the short-time/long-time averaging (STA/LTA)-based beamforming approach described by Verdon et al. (2017) to locate additional events. A velocity model derived from a nearby vertical well was used subsequently to calculate hypocentre locations. Applying quality-control criteria based on the observed stacking power, as described by Verdon et al. (2017), we successfully located 18,472 events (Figure 2). This catalog has over ten thousand events between magnitude –2 and 0, with a magnitude of completeness of –0.2. The improvement in event detection produces a significant increase in the detail provided by the microseismic observations.

2.2 Event Locations

A map of the 18,472 located events is shown in Figure 2. The coloured circles correspond to the events during the stimulation of Well C, while the grey dots represent events that occurred afterward during the stimulation of Wells A, B and D. There were 125 stages during Well C,

with an average injection volume per stage of 500 m^3. The hydraulic fracturing proceeded from the toe of Well C (i.e. the northernmost end) to the heel.

Microseismicity that is directly linked to hydraulic fracture propagation, known as operationally induced microseismicity (Eaton, 2018), occurs during (or shortly after) active injection stages. Such events are generally characterized by sub-zero moment magnitudes and typically form elongate clusters aligned parallel to the maximum principal stress direction, *SHmax*, tracking the propagation of hydraulic fractures (Eaton, 2018). Based on the design of the hydraulic fracturing stimulation in this study, we expect to see bi-wing hydraulic fracturing events within ~200 m of each stage in a symmetrical distribution in both directions. However, due to the magnitude of completeness for the monitoring array, many of the stages appear to have limited associated microseismicity. In particular, the first 20 stages have few events within the immediate vicinity of the wells. Instead, two structures are illuminated by the microseismicity during this time, which are oriented at N30˚E, oblique to the regional *SHmax* orientation (N44ºE - N64ºE, see below). These two features appear to be mutually aligned and are labelled as SW1 in Figure 1 (South-West striking fracture network 1). Both SW1 clusters extend up to 600 m away from the well, which is significantly farther than normally anticipated for hydraulic fracturing (Maxwell et al., 2010). As the hydraulic-fracturing stages proceeded southwards along the well, the locus of microseismicity migrated along this structure, moving progressively to the southwest.

This same behaviour is apparent along another four structures, all of which are parallel, striking at N30˚E (labelled SW2 – SW5). For each of these structures, microseismicity initiated in the northeast and propagated to the southwest as the active hydraulic fracturing stages moved southwards along the well. This spatiotemporal evolution is inconsistent with expectations for operationally induced microseismicity, which generally initiates at the well and migrates outwards. This atypical behaviour is investigated further below.

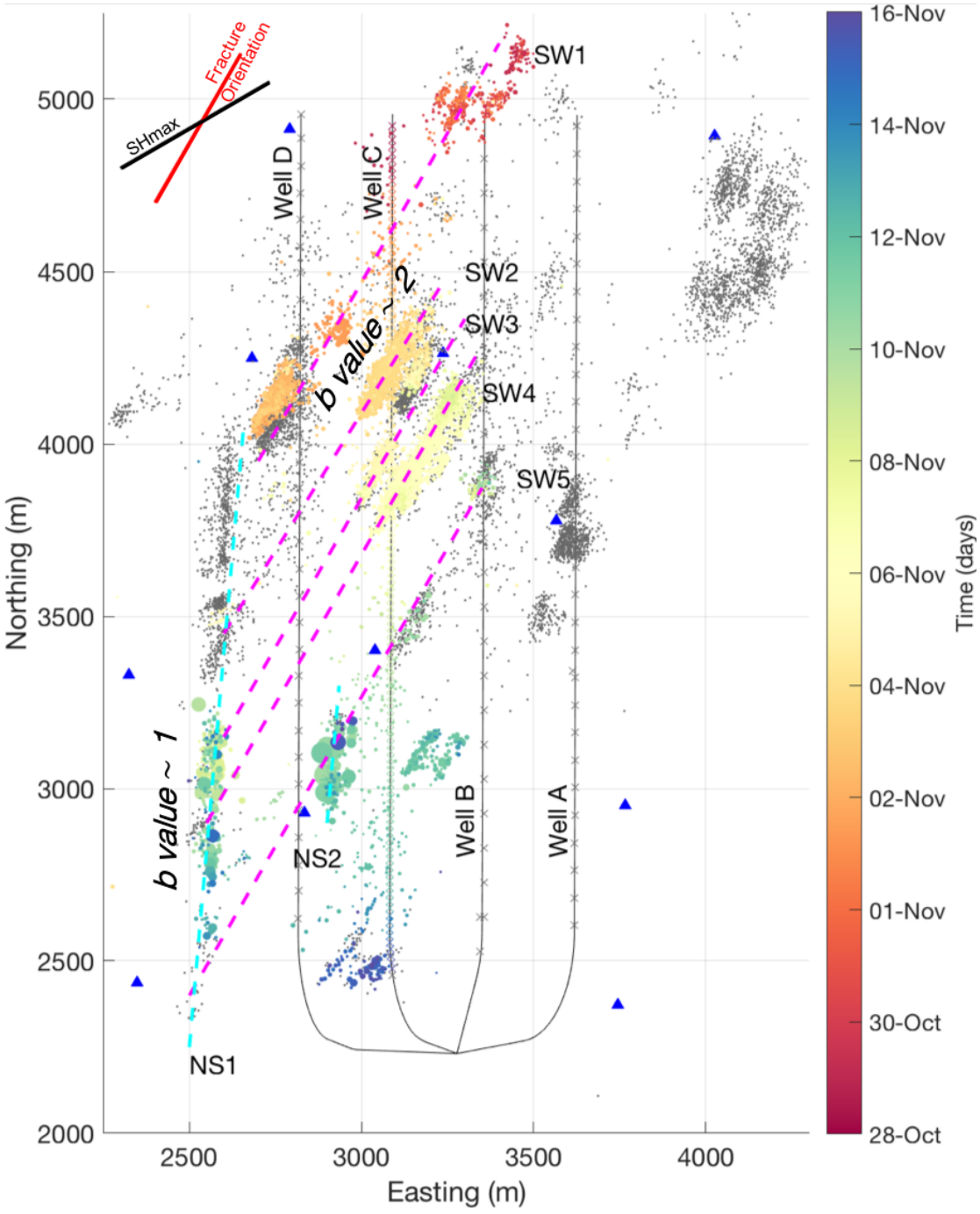

219

220 *Figure 2: Map of events recorded during hydraulic stimulation of Well C (dots coloured by occurrence*
221 *time) and during stimulation of Wells A, B and D (grey dots) at the ToC2ME site. Blue triangles are a*
222 *subset of the borehole array stations, x symbols at the wells are the locations of the stages. Well C was*
223 *the first to be stimulated, with hydraulic fracturing treatments taking place along its full length. Features*
224 *delineated by the microseismic activity are annotated: the large, N-S trending fault, NS1, runs roughly*
225 *500 m to the west of Well C, while a smaller N-S fault NS2 is closer to Well C. Five discrete clusters*
226 *trending N30°E (SW1 – SW5) extend east and west of Well C. Dashed magenta lines show the*
227 *extrapolation of these features to NS1.*

Another significant feature is located approximately 500 m west of Well C. This structure (NS1: north-south fault 1) is oriented at N5˚E, and ultimately grew to become a 1.5 km long lineation. All of the largest magnitude events occurred along NS1. A smaller north-south trending structure, NS2, is also apparent towards the south end (heel) of the well, and approximately 200 m to the east. This feature appears to intersect the inferred SW5 structure.

In the second half of the stimulation program, Wells A, B and D were hydraulically fractured concurrently, with stages alternating between wells and progressing from north to south. During this activity, the SW1 – SW5 features were reactivated, in addition to several NE-SW trending features further to the east. The northern portion of NS1, which was quiescent during stimulation of Well C, also experienced activity during the stimulation of wells A, B and D. However, these events in the northern portion of NS1 are not the focus of our study, since our objective is to examine how this linear feature, inferred to be a fault, was initially activated by hydraulic-fracturing operations.

2.3 Interpretation of Key Structures

To further investigate the key structures described above, we consider the Gutenberg-Richter *b*-values of magnitude-frequency distributions, the seismicity depth distribution, event locations and occurrence times relative to active injection stages.

The linear NS1 feature is interpreted as a strike-slip fault. This cluster hosts the largest events, with magnitudes up to M_W 3.2 and right-lateral strike-slip mechanisms (Zhang and Eaton, 2019). Based on a maximum-likelihood estimate of the slope of the magnitude-frequency distribution (*b* value), Igonin et al. (2018) estimated that $b \sim 1.12$ for events along this feature. Cases of $b \sim 1$ may be indicative of the release of tectonic stresses on a large, planar structure (e.g., Verdon et al., 2013). Taken together with the overall length of NS1 (> 1.5 km), we interpret this feature as a pre-existing fault that was sequentially activated during hydraulic fracturing. Similarly, seismicity along NS2 is characterized by $b \sim 1.10$ (Igonin et al, 2018); based on this *b* value and its strike direction parallel to NS1, we infer that NS2 is likely to be a fault that is genetically related to NS1.

For both NS1 and NS2, careful analysis of focal depths of the associated seismicity (Supplementary Material) shows that nearly all of these events are located within the Ireton shale, above the target Duvernay Formation (Figure 3). This stratigraphic and depth relationship is robust, as the event depths were determined using a new technique that correlates arrival-time picks with 3D multi-component (converted-wave) seismic observations (Poulin et al., 2019). In cases where 3-D multicomponent seismic observations are available, this method

leverages unambiguous time-depth information derived from correlation of reflections observed in the P-P and P-S seismic datasets (Poulin et al., 2019).

The seismicity associated with the SW1 – SW5 structures is also depth-located within the overlying Ireton Formation (Figure 3), although a small subset of these events is located in the Duvernay Formation. Within-zone events also occur along the track of Well C, in spatial and temporal proximity to the corresponding injection stage. We infer that this event subset, within the target formation and near the injection point, is operationally induced microseismicity that is directly associated with hydraulic fracturing. We expect such microseismicity to have relatively low magnitudes, which limits the number of these events that are detectable; hence details including hydraulic-fracture orientation are difficult to discern clearly.

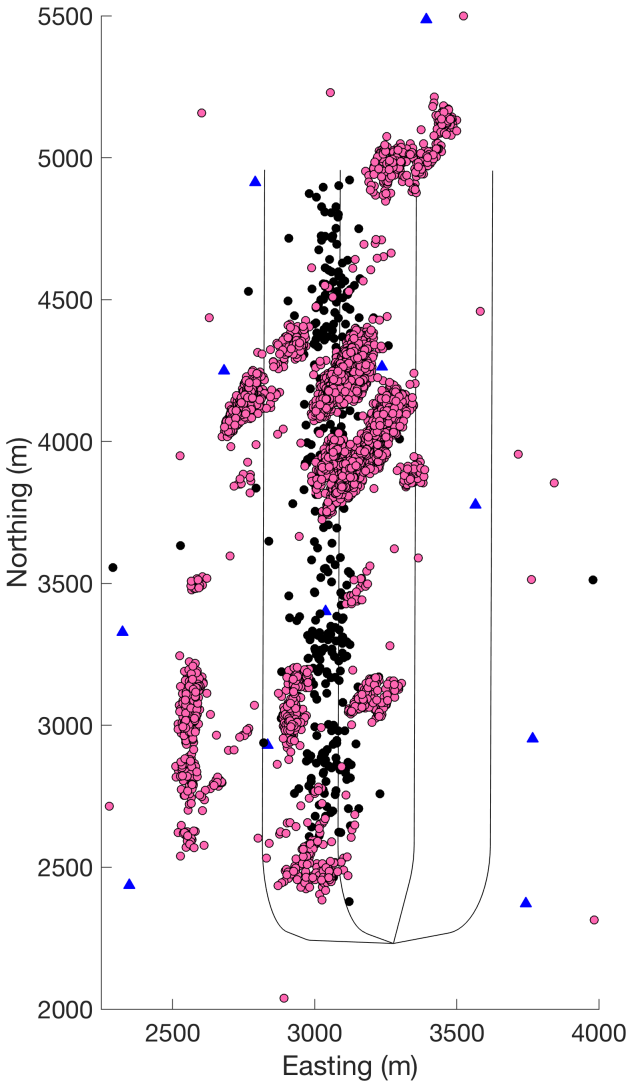

Figure 3: Depth difference between inferred hydraulic-fracturing events (black circles) and induced seismic events (pink circles). The depths of the HF events are within the targeted Duvernay Formation, but other events (possibly induced) are shallower, and occur within the overlying Ireton Formation.

We now turn our attention to the SW1 – SW5 structures. In Figure 3 event populations are coloured by depth to indicate whether hypocentres are located in the Duvernay or the overlying Ireton Formation. The SW structures are primarily concentrated in the Ireton shale, above the hydraulic-fracturing zone. The estimated *b* values for the SW clusters are $b \sim 2.54$ for the NE portion of SW1, $b \sim 2.18$ for the SW portion of SW1, and $b \sim 1.82$ for SW2, SW3 and SW4 combined (Igonin et al., 2018). These elevated *b* values are inconsistent with activation of large fault structures, but may be indicative of seismicity driven by fluid pressure perturbations within distributed fracture networks (e.g., Verdon et al., 2013).

There are several observations that indicate that these clusters of seismicity are not directly related to hydraulic fracture growth. Firstly, their orientation at N30^{o}E is oblique (by 15 - 30^{o}) to *SHmax*, the expected orientation of seismicity clusters that form near hydraulic fractures (Eaton, 2018). Secondly, the majority of event depths are well above the stimulation zone, contrary to expectations for operationally induced microseismicity. Moreover, these zones were reactivated during subsequent stimulation in wells A, C and D, which is not generally observed during hydraulic fracturing. Finally, hydraulic fractures always initiate at the well and grow outwards, whereas the observed pattern of seismicity exhibits retrograde behaviour, initiating in the northeast and migrating toward the well. Collectively, these lines of evidence indicate that seismicity within clusters SW1-5 is not directly related to hydraulic-fracture growth.

Here, we consider an alternative hypothesis, namely that features SW1-5 represent migrating zones of seismicity along natural fracture corridors (e.g., Questiaux et al., 2010; Peacock et al., 2016). According to this model, pre-existing natural fracture systems in the overlying Ireton Formation were activated by pressure increases caused by hydraulic fracturing in the Duvernay Formation. The presence of large-scale natural fracture systems at this location and depth is consistent with a structural model for ToC2ME, proposed by Eaton et al. (2018), in which the four HF wells are located in a flower structure that formed during the Devonian within step-over zone between basement-rooted strike-slip faults. A regional flower-structure model has also been proposed to explain patterns of induced seismicity in other nearby studies of hydraulic fracturing in the Duvernay Formation (Wang et al., 2018; Eyre et al., 2019). Flower structures often contain internal fracture systems (Riedel shears) that are oblique to the primary strike-slip faults (Huang and Liu, 2017). We remark that the orientation of the linear event distributions in SW1-5 is also oblique, by approximately 30^{o}, from the *SHmax* direction (N60^{o}E) calculated by Zhang and Eaton (2019) based on stress inversion of moment tensors. Taken together, this means that such fractures would be critically stressed, a condition that is conducive to fluid flow (Rogers, 2003).

In summary, the foregoing observations and discussion lead to the following interpretive classification scheme:

1. Fault activation (NS1, NS2): Based on a *b* value of ~1, occurrence of large events, and large, linear structure;
2. Fracture network activation (SW1-SW5): Based on *b* values ~2, temporal evolution of events along the structure from NE to SW (rather than growth outwards from the well), apparent misalignment with *SHmax*, and depth above the zone of interest;
3. Operational microseismicity: Based on the timing of the stages and focal depths within the zone of interest.

In the following sections, we apply this classification scheme to develop a model that fits the observed pattern of induced seismicity.

2.4. Determination of principal stress direction

On a regional scale in Alberta, there is a generally uniform maximum horizontal stress direction of *SHmax* ~ 45° (Heidback et al., 2016). However, in the vicinity of the ToC2ME program, the *SHmax* orientation varies from 44°-64°. One of the likely reasons for this variability is proximity to carbonate platforms, which have been shown in previous studies to have a significant control on the stress field orientation (e.g. Viegas et al., 2018). Since our dataset was acquired within a few kilometres of known reef/platform edges, additional data was used to determine the local stress conditions.

Zhang et al. (2019) computed focal mechanisms for a subset (530 events) of the ToC2ME dataset, a subset of which are shown in Figure 4. For the events in clusters NS1 and NS2 they found right-lateral strike-slip mechanisms, with one of the nodal planes oriented N-S, while for the events in the SW1 – SW5 clusters they found right-lateral strike slip mechanisms with one of the nodal planes oriented at 30°. The nodal plane strikes are consistent with the orientations of the event clusters. Zhang et al. (2019) used these focal mechanisms to estimate the *in situ* stress field using a linear stress inversion method (Michael, 1984), finding *SHmax* ≈ N60°E. This value is up to 15° from the regional stress direction, but is consistent with the nearest *in situ* observation and within the range of WSM stress orientations observed in the local area. Indeed, the closest WSM measurement point is 59 degrees. Due to the uncertainty in the inversion, we posit that the *SHmax* direction is likely to be closer to 60° than the regional strike (45°), acknowledging that the proximity to the reef edges may add local complexity to the stress field.

We do not observe clusters of microseismicity that are aligned parallel to the *SHmax* direction, which is the expected orientation for operationally induced microseismicity during hydraulic fracturing (e.g., Eaton, 2018). As described above, we infer that most of the microseismicity that is directly associated with hydraulic fracturing falls below the detection limits of the methods used here. In contrast, when hydraulic fractures intersect faults or fracture corridors this gives rise to larger, detectable events, with both the cluster orientation and the focal mechanisms aligned along the orientation of the activated feature.

2.3. Imaging fracture networks using seismic anisotropy

Seismic anisotropy is the measure of the magnitude and direction of shear-wave splitting of earthquakes. The magnitude of the seismic anisotropy signifies the amount of anisotropic media that the wave front travelled through between the source and receiver. The direction of seismic anisotropy, or the fast S-wave orientation, is influenced by two factors: 1) stress direction (i.e. *SHmax*), and 2) subsurface structure. To image the seismic anisotropy at the site we used the method of Teanby et al. (2004) to measure S-wave splitting on the 300 largest-magnitude events, since these had the best signal to noise ratios, and clear P- and S-wave picks on all or most stations. We made a total of over 20,000 individual S-wave splitting measurements (300 events recorded at 69 stations), but quality-control criteria (Teanby et al., 2004) reduces this to a population of 7,818 good quality measurements.

The fast S-wave orientations, ψ, are plotted at each receiver (although they actually represent the path-averaged anisotropy between their respective sources and receivers) in Figure 4. There is variation in ψ over the array footprint, with ψ oriented N-S to the south east of the array, but becoming more E-W to the NE of the array. However, around the wells themselves, ψ is relatively consistent at approximately 30°. This is a close match to the orientations of the SW1 – SW5 clusters, which we infer to be fracture corridors. It is roughly 30° from the estimated *SHmax* orientation of N60°E (see above). For this reason, we interpret the fast S-wave $\psi = 30°$ as being caused by aligned fractures within the Ireton formation. At 30 degrees from *SHmax*, these parallel fracture sets would be optimally oriented for failure.

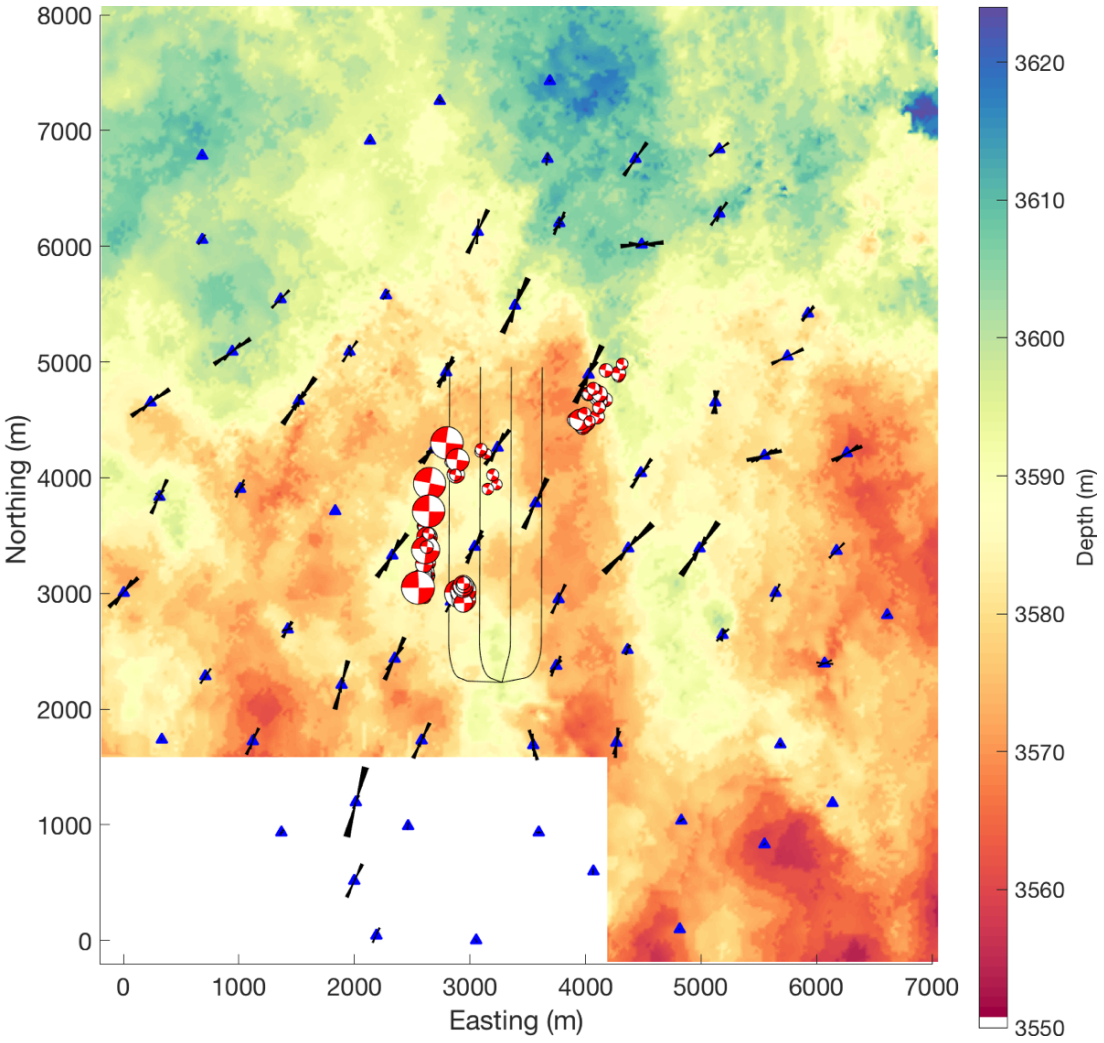

Figure 4: Map view of anisotropy observed using S-wave splitting analysis. Fast S-wave directions are plotted as rose diagrams at each station and focal mechanisms for the 100 largest events are shown at their respective event locations. Background contours show the depth structure of the Beaverhill Lake Group formation. Focal mechanisms for a subset of events computed by Zhang et al. (2019) are also shown.

A 3D multicomponent reflection seismic survey acquired at the site provides further information about faults at the site. Figure 4 shows the depth to the top of the Beaverhill Lake Group formation, which underlies the Duvernay. Significant depth discontinuities mark the positions of dip-slip faults that extend from the Pre-Cambrian basement through to the Duvernay (Eaton et al., 2018). In particular, a large fault trending roughly N-S can be seen just to the east of Well A. It is rooted in the basement and is thought to have formed during extensional rifting in the Precambrian (Ekpo et al., 2017). However, this feature does not appear to re-activate during injection. No clear structure associated with the NS1 fault can be seen in the 3D seismic. This would not surprising if this is a strike-slip feature, since it would not

produce detectable offset of horizontal beds. Similar reactivation of faults that are not detectable with 3D seismic data has been documented elsewhere (e.g., Clarke et al., 2019).

Based on 3-D seismic data (Eaton et al., 2018), the observed faults are interpreted to be basement rooted (i.e. they extend downwards into the Precambrian basement). However, there is no indication of seismicity extending into the basement (see Supplementary Material). This behaviour contrasts with induced earthquakes in Oklahoma and Ohio, where the largest earthquakes have been shown to occur in the basement, both due to wastewater injection (Ellsworth, 2013), and hydraulic fracturing (Kozłowska et al., 2018).

3. Interpretation: Position and Timing of Fault Reactivation

We investigate fault-activation processes by examining the timing and position of reactivation within the various clusters relative to positions of HF stages. In Figure 4 we provide a more detailed view of the seismicity associated with the SW2 – SW4 structures, from stages 30 to 80. An animation of the seismicity sequence is provided in the online Supplementary Materials. In addition to the observed microseismic events, we plot ellipses with long axes oriented at 60°, centred on each perforation interval. These are included to delineate the assumed positions of the hydraulic fracture zones, which are not clearly imaged by the microseismic events. The key times within the sequences of microseismicity are also listed in Table 1.

Time	Stage No.	Processes
Oct 31st, 23:00	7	Activity begins in SW1 cluster
Nov 2nd, 23:00	29	Activity begins in SW2 cluster
Nov 4th, 18:00	47	Activity begins in SW3 cluster
Nov 4th, 20:00	48	Activity begins on the NS1 fault, at a position in line with the SW2 cluster
Nov 5th, 07:00	53	Activity begins in the SW4 cluster
Nov 7th, 10:00	64	Activity on the NS1 fault shifts southward to a position in line with the SW3 cluster
Nov 8th, 18:00	73	Activity begins in the SW5 cluster
Nov 9th, 03:00	77	Activity on the NS1 fault shifts southward to a position in line with the SW4 cluster
Nov 9th, 23:00	87	Activity begins on the NS2 fault where it is intersected by the SW5 cluster
Nov 12th, 20:00	115	Activity on the NS1 fault shifts southward to a position in line with the SW5 cluster.

Table 1: Sequence of processes that occur during the stimulation, as illuminated by the microseismicity.

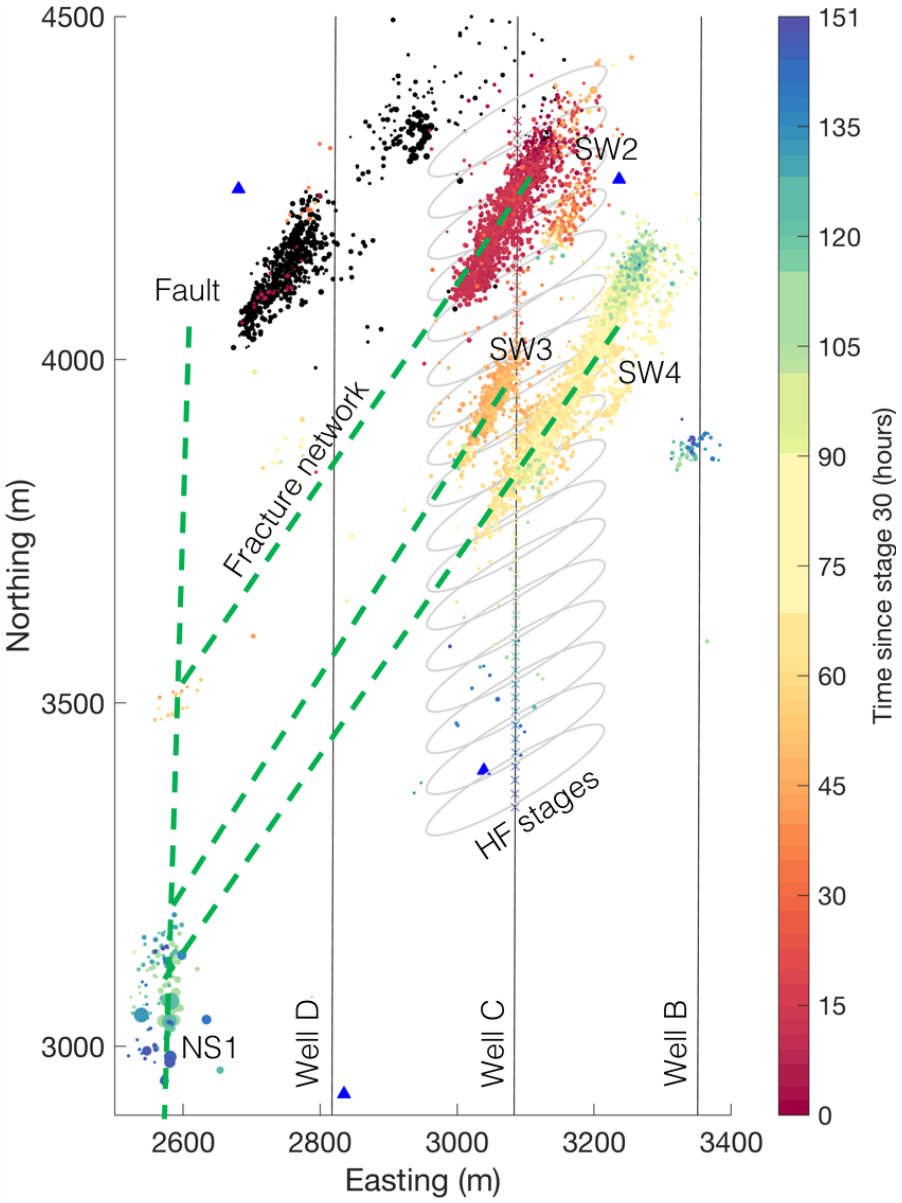

402

403 *Figure 5: Snapshot of activity along well C between stages 30 and 80. Black dots show the*
404 *events that had occurred before the snapshots; coloured dots show events that occurred during*
405 *the specified time period. Dashed green lines highlight activated features at 30 degrees. The*
406 *grey ellipses show the assumed positions of the hydraulic fractures (trending parallel to SHmax*
407 *with a length of 150 m) from each stage.*

408 Seismicity on SW2 began at approximately 23:00 on the 2016/11/02, whereas activity began
409 on the SW3 structure at 18:00 on 2016/11/04. The first events on the NS1 fault are also seen
410 shortly afterwards at 20:00 on 2016/11/04. However, the positions of these first events on the
411 NS1 fault are aligned with the SW2 cluster, i.e. they occur at the point where linear
412 extrapolation of the SW2 cluster intersects the NS1 fault. The lateral distance from the active

stage at this time, Stage 48, to the first NS1 events is approximately 800 m; in addition, these NS1 events do not align with a continuation of the Stage 48 position along the *SHmax* direction

As stimulation proceeded, activity continued in the SW3 cluster, and began in the SW4 cluster as it is intersected by the stimulation zones at 07:00 on 2016/11/05. At 10:00 on 2016/11/07, further activity occurred on the NS1 fault, with events located several hundred meters south of the first events. The new locus of reactivation on NS1 is aligned with the SW3 feature and is approximately 900 m from the position of the active stage. The events on the NS1 fault again do not align with a continuation of the active stage position along the *SHmax* direction, but occurred in a position at which linear extrapolation of one of the SW clusters intersects the NS1 fault. By 03:00 on the 2016/11/09, the loci of seismicity has again shifted southwards on the NS1 fault, to a position aligned with the SW4 cluster.

The same pattern of behaviour is observed as stimulation reaches the southernmost SW5 cluster. This feature began to reactivate when intersected by the hydraulic stimulations at 18:00 on the 2016/11/08. Activity on the smaller NS2 fault began where it intersects the SW5 cluster at 23:00 on 2016/11/09, and activity is observed on the NS1 fault, at a position that is in alignment with the SW5 structure, at 20:00 on the 2016/11/12.

Therefore, the timing and position of the seismicity on the NS1 fault are consistent with a model wherein fault activation is controlled by the positions of the SW-trending fracture corridors. When the NS1 fault was initially activated, it did so in a position that is directly aligned with the SW2 cluster (Figure 2). Subsequently, the loci of activity shifts southwards along NS1, where each shift in position was aligned with each of the SW clusters in space, but lags in time. We therefore interpret that the SW2 – SW5 fracture corridors represent permeable pathways, transmitting elevated pore pressures from the well to the NS1 and NS2 faults. There is a time delay between the activation of each SW cluster at the well, and the occurrence of seismicity at the corresponding position on NS1 (see Table 2). This time delay may correspond to the time elapsed as elevated pressures diffused along the SW-trending fracture corridors, reaching and reactivating the NS1 fault. The distribution of microseismic events observed along the SW2 – SW5 clusters does not extend as far as the NS1 fault. Our interpretation is that the pore pressure perturbation is communicated, in part, aseismically, or at least without generating seismic events above the detection limits of the monitoring array. Nevertheless, that the SW2 – SW5 structures extension to the NS1 fault can be inferred from the loci of seismicity on NS1 being aligned with these features.

	Time activation begins at well	Time activation on corresponding part of NS1 begins	Time delay (hours)
SW1	Oct 31st, 23:00	NA	NA
SW2	Nov 2nd, 23:00	Nov 4th, 20:00	44
SW3	Nov 4th, 18:00	Nov 7th, 10:00	64
SW4	Nov 5th, 07:00	Nov 9th, 03:00	92
SW5	Nov 8th, 18:00	Nov 12th, 20:00	98

Table 2: Delay times between the onset of activity in each of the SW clusters, and the onset of activity on the corresponding segments of the NS1 fault.

4. Investigating Possible Mechanisms for Fault Reactivation

In the preceding sections, we have identified trends in the microseismic data that show evidence that fracture networks play a key role by providing a conduit for pressure perturbation that leads to seismicity on a nearby fault. To test the feasibility of this mechanism, we generate simple representative models for this scenario. We note that our objective here is not to provide a definitive constraint on the properties of the fracture corridors, but simply to show that reasonable values for the corridor's dimensions and flow properties can generate plausible perturbations at the fault, both in terms of the time at which the perturbation arrives, and the magnitude of the perturbation. We also discuss the possibility of event triggering through poroelastic stress transfer, and from transfer of stress from the events observed on the SW2 – SW5 clusters.

4.1. Fluid-flow modelling

To investigate whether fluid flow along pre-existing fracture corridors is a plausible mechanism for fault reactivation, we model the expected diffusion of pressure along a fracture corridor. Initially we approach the problem analytically, using the concept of seismic diffusivity. Talwani and Acree (1985) studied a series of reservoir-impoundment induced earthquakes. Their observations of delay times between reservoir lake levels and seismicity, and of increasing epicentral areas with time, led them to conclude that pore pressure diffusion was the causative mechanism. They applied the concept of seismic hydraulic diffusivity, α_s, which describes the relationship between the event occurrence time t, and the distance between the event and the pore pressure source L:

$$\alpha_s = \frac{L^2}{t}. \quad (3)$$

Along the 30° orientation mapped by the SW clusters, the NS1 fault is located roughly 800 – 1,000 m from Well C. The events on the NS1 feature commence from between 44 to 98 hours after activation of each of the respective SW clusters (Table 2). Using these parameters in Equation 2, we arrive at values of $2.8 < \alpha_s < 7$ m^2/s, well within the range of values described by Talwani and Acree (1985), who found values of $0.5 < \alpha_s < 60$ m^2/s for a variety of geological settings, with most values clustering around 5 m^2/s.

The permeability of a fracture corridor, κ_{FC}, can be computed from the diffusivity using (Brace, 1980):

$$\kappa_{FC} = \frac{\alpha_s \eta \phi}{K}, \quad (4)$$

where η is the fluid viscosity, ϕ is the porosity, and K is the fluid bulk modulus. Because we do not know the properties of fluids that saturate the fracture corridors, we consider cases of both gas and water. We use the Batzle and Wang (1992) equations to compute the properties of gas with a specific gravity of 1, and brine with a salinity of 100,000 ppm, at a temperature of 100°C and a pressure of 38 MPa, and use a value for porosity of $\phi = 6.5\%$. These values are a very generic representation of conditions in the Ireton (e.g., Dunn et al., 2012; Lyster et al., 2017). Use of these values in Equation 4 yields an analytic solution with values of κ_{FC} varying from 25 – 100 mD.

To incorporate greater complexity including multiple stages of injection at different times and locations we address the problem numerically using a commercial reservoir simulation code Tempest (Emerson, 2014). We create a model that represents our inferred system – hydraulic fractures intersecting a fracture corridor that transfers pressure increases – in a simplified form. Tempest simulates fluid flow through porous systems but does not simulate the coupled hydro-geomechanical behaviour of HF propagation. Instead, we pre-insert the hydraulic fractures and a fracture corridor into the model. This simplification is reasonable because our primary aim is to model fluid and pressure propagation along a pre-existing fracture corridor, rather than to simulate the HF propagation itself. Whereas developing a hydro-geomechanical simulation is complex from a modelling perspective, reservoir fluid flow models are relatively simpler to populate and utilise. Similarly, while in reality the permeability of a fracture corridor will be pressure-dependent, we do not simulate this effect in our model.

The model setup is shown in Figure 6. The background shale rock has a permeability of κ_S = 0.005 mD (Ghanizadeh et al., 2015a). We simulate 11 individual HF stages with a horizontal spacing of 20 m, representing roughly the number of stages that appear to be associated with

reactivation of each SW-trending fracture corridor based on the observed microseismicity. Based on the operational records (Eaton et al., 2018), we model 400 m^3 of water injected over a 3-hour period for each stage, with a 1 hour gap between each stage. Each stage connects to a HF with a permeability of 1,000 mD, a half-length of 150 m and a height of 120 m, running at 60° to the well trajectory. The fracture corridor to which the hydraulic fractures connect has a length of 1,200 m, width of 5 m, and a height of 300 m, running at 30° to the well trajectory. The fracture corridor is intersected by each of the hydraulic fractures that extend from the well. Using our analytical results as a starting point, we vary κ_{FC} from 50 – 1,000 mD. Full model details are provided in the Supplementary Materials.

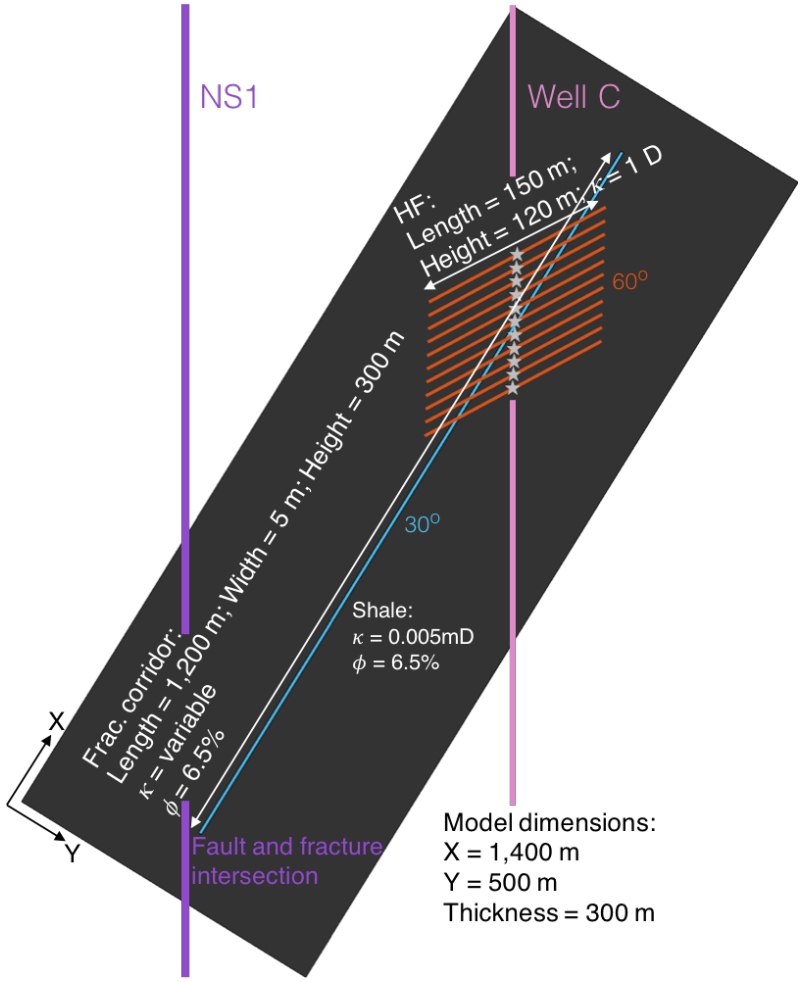

Figure 6: Schematic representation of our fluid flow model: 11 HF stages (orange lines) are simulated, which connect into a fracture corridor (blue line) with a length of 1,200 m and a width of 5 m. The change in pore pressure is measured at the intersection of the fault (purple line) and fracture.

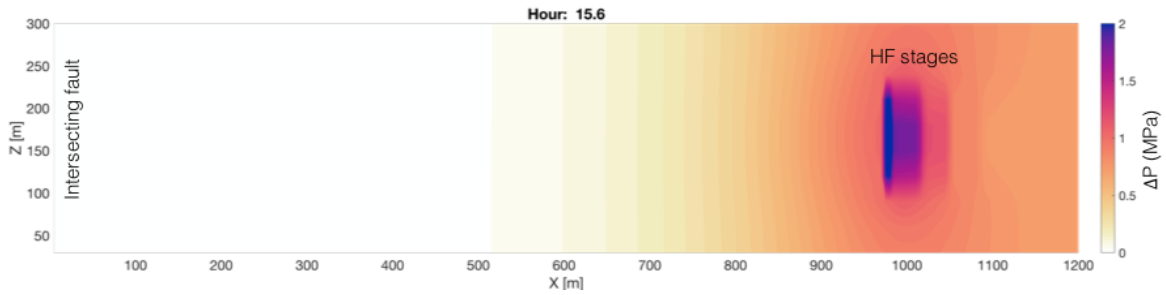

Figure 7: Modelled change in pore pressure (in MPa) at a single time-step (T = 15.6 hours) along the fracture corridor: pressures are elevated where the HF intersects the fracture corridor (at X = 980 m) and the pressure pulse thereupon propagates along the feature.

Figure 7 demonstrates an example model instantiation (κ_{FC} = 100 mD), showing the distribution of pore-pressure changes along the fracture corridor at a single model time-step (an animation showing the pressure evolution along the fracture corridor as a function of time is provided in the online Supplementary Materials). Pressures become elevated where the active HF intersects the fracture corridor – this pressure pulse then propagates along the length of the fracture corridor.

Our primary interest is the pressure change at the distal end of the fracture corridor, where it would intersect the NS1 fault. In particular, we are interested in the magnitude of any pressure increase, and its timing relative to the injection stages, as this will indicate whether (i) the modelled pressure changes are sufficient to cause fault reactivation, and (ii) whether the timing of pressure increase is commensurate with the observed time delays between initial reactivation of the SW clusters near to the well and the onset of activity on the NS1 fault.

Figure 8 shows curves representing models with varying values of κ_{FC}. In each case we observe an increase in pressure, the magnitude and timing of which is strongly dependent on the fracture corridor permeability. The magnitude of the pressure increase, ΔP_{MAX}, is larger for higher permeabilities, with the largest increase of ΔP_{MAX} = 0.85 MPa occurring for κ_{FC} = 1,000 mD, and the smallest increase of ΔP_{MAX} = 0.45 MPa occurring for κ_{FC} = 50 mD.

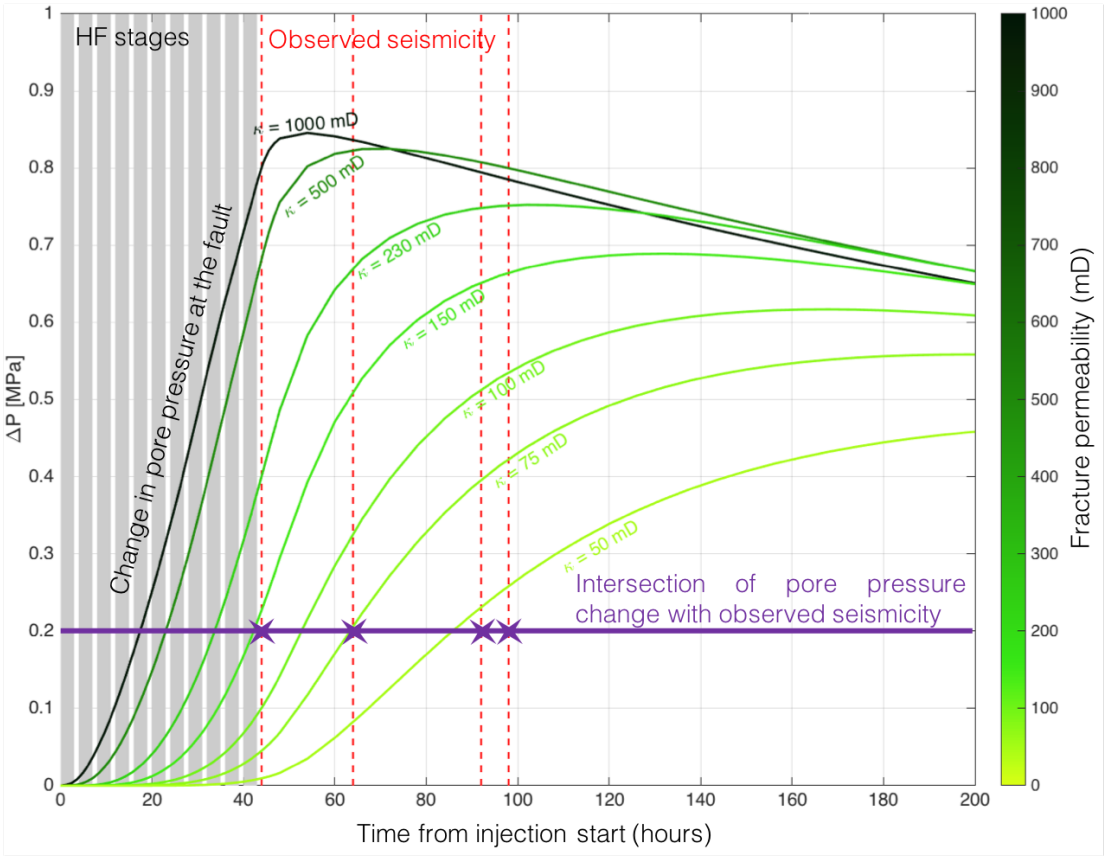

Figure 8: Modelled pore pressure increases at the distal end of the fracture corridor as a function of time, for a suite of fracture corridor permeabilities from 50 – 1,000 mD. The 11 injection stages are marked by the grey shading, while the observed reactivation times of the NS1 fault from the onset of activity on each SW fracture corridor are marked by the red dashed lines. The green curves represent the change in pore pressure at the fault, at a lateral distance of 1 km, given the different values of fracture zone permeability. The horizontal purple line and purple stars indicate the intersection between an example pore pressure change of 0.2 MPa at the fault and the observed seismicity.

This range of pressure increases is much larger than that modelled by Keranen et al. (2014) for the Jones, Oklahoma earthquake swarm, but is similar to that calculated by Schoenball et al. (2018) for the Guthrie-Langston, Oklahoma, earthquakes. It is also significantly larger than static stress transfer magnitudes that have been invoked as causes for fault activation elsewhere (e.g., Pennington and Chen, 2017; Kettlety et al., 2019). Evidently, the range of pore pressure increases produced by our model, regardless of κ_{FC}, are within (or above) the range typically deemed sufficient to cause fault reactivation.

The time delay between the start of injection and the maximum pressure increase at the distal end of the fracture, T_{PMAX}, is smaller for higher permeabilities, with the smallest delay time of T_{PMAX} = 52 hours for κ_{FC} = 1,000 mD, and the largest delay time of T_{PMAX} = 250 hours occurring

554 for κ_{FC} = 50 mD. Once ΔP_{MAX} has been reached, pressures gradually decrease as fluids diffuse
555 into the non-fractured shale rock mass.

556 In Figure 8 the pressure increases with time are compared with the observed time delays
557 between the onset of activity in each SW cluster and activity in the corresponding portion of
558 the NS1 fault (Table 2, red dashed lines in Figure 8). Consider an example pore pressure change
559 of 0.2 MPa at the fault (purple line in Figure 8). For the lower permeability cases (κ_{FC} = 50 mD
560 and κ_{FC} = 75 mD), the changes in pore pressure after 40 hours (the shortest observed
561 reactivation delay time) are negligible. This would appear to rule out these lower κ_{FC} models,
562 since elevated pressures are not able to reach the fault by the time that it is observed to
563 reactivate.

564 For the κ_{FC} = 1,000 mD case, pressures at the distal end of the fracture corridor increase rapidly,
565 and have reached almost their maximum value by the shortest observed reactivation delay time
566 (40 hours). In this case we would expect to have observed seismicity much sooner, but that is
567 not the case. Moreover, the modelled pressures are decreasing by c. 90 hours, corresponding to
568 the largest observed reactivation delay time, which would appear to rule out these models since
569 we would expect reactivation to occur while pressures are increasing. However, the higher
570 permeability models cannot be ruled out entirely, as delays between the reactivation trigger and
571 the resulting seismicity have been observed (e.g., van der Elst et al., 2013), implying that the
572 time delay between the modelled increase in pressures along the fracture zone and the observed
573 seismicity on the fault is caused by the gradual nucleation of rupture on the fault before
574 observed seismicity takes place.

575 Based on these models, the mid-range permeability models (κ_{FC} = 150 – 230 mD) show the
576 best match to the observed reactivation delay times. The pressure has increased by a substantial
577 amount (> 0.2 MPa) by 44 hours (the shortest observed reactivation delay period) and is
578 continuing to increase, reaching near to the maximum by 90 – 100 hours (the longest observed
579 reactivation delay periods). Although these permeabilities are several orders of magnitude
580 larger than the matrix permeability, laboratory tests of the permeability of unpropped fractures
581 in the Montney formation of Alberta, Canada, yield even larger fracture permabilities on the
582 order of 1-3 Darcies (Ghanizadeh et al., 2015b).

583 In summary, both the analytical and numerical modelling demonstrates that the observed delay
584 times are consistent with pore pressure transfer along a fracture corridor, assuming permeability
585 values that are consistent with observations of seismic hydraulic diffusivity made in a range of
586 geological settings (Talwani and Acree, 1985). Numerical modelling indicates that pore

pressure increases of 0.5 MPa might reasonably be expected at the fault assuming such a mechanism.

4.2. Stress transfer

Deformation and slip around Well C produced by hydraulic fracturing will affect the stress field in the surrounding rocks. If this produces Coulomb Failure Stress (CFS) increases on the NS1 fault, then this stress transfer represents a viable alternative causative mechanism for the induced seismicity. There are two potential sources for stress transfer onto the NS1 fault. The first is elastostatic stress transfer due to the tensile opening of the hydraulic fractures (e.g. Kettlety et al., 2020), and the second is the seismicity occurring in each of the SW clusters.

4.2.1. Stress Transfer caused by tensile hydraulic fracture opening

The tensile opening of the hydraulic fractures is more challenging to model, since this process is mostly aseismic (e.g., Maxwell et al., 2008), and so we do not have any observations that directly constrain either the orientations or the lengths of the hydraulic fractures, nor the amount of opening that has occurred. Instead, we appeal to an observational argument to assess whether stress transfer from hydraulic fracture opening could be causing reactivation of the NS1 fault.

Hydraulic fracturing takes place along the length of Well C from toe to heel, using a very similar injection design for each stage. We can surmise that any zones of increased CFS associated with tensile opening would also move consistently southwards as Well C is stimulated. If stress transfer from tensile hydraulic fracture opening was the cause of seismicity on the NS1 fault, then we would expect the fault to reactivate along its entirety, with the loci of seismicity moving consistently southwards along the fault. Instead, as documented in Section 3, seismicity occurs at specific points along the fault that are aligned with the SW clusters.

The behaviour of the NS1 fault during stimulation of Well C can be contrasted with the behaviour during stimulation of Well D, which is within 200 – 300 m of the fault. During stimulation of Well D, the NS1 fault reactivates along its entire length, with the loci of seismicity moving consistently southwards as the hydraulic stimulation moves southwards along Well D, as might be expected if there is direct interaction between the hydraulic fractures and the fault.

We also note that models of poroelastic stress transfer generated by tensile fracture opening (e.g., Westwood et al., 2017; Kettlety et al., 2020) have found changes in the CFS at distances

larger than 500 m to be significantly smaller than the pore pressure changes modelled in Section 4.1.

4.2.2. Stress Transfer caused events in the SW clusters

An alternative possibility is that slip on the NS1 fault could have promoted inter-event triggering through the mechanism of static stress transfer. Modelling of stress transfer caused by earthquake slip is well established, having its origins in understanding aftershock distribution after large tectonic earthquakes (e.g. Stein et al., 1992). Here we use the PSCMP code (Wang et al., 2006) to model the changes in CFS caused by the events in each of the SW clusters.

This modelling requires the rupture dimensions and orientation to be specified. Such parameters can only be directly constrained for a small fraction of the events with the highest signal to noise ratios (e.g., Zhang et al., 2019). Instead, we approach the problem from a stochastic perspective (e.g., Verdon et al., 2015). We know the position of each event, and the event magnitudes. We assign source mechanism parameters to each observed event in each cluster randomly from appropriate statistical distributions. We perform 1,000 model instantiations for each of the SW clusters, taking as our result the median stress changes from the overall model population.

Zhang et al. (2019) show that all the events within the SW clusters have right-lateral strike-slip mechanisms, with vertical nodal planes striking at 30^o (parallel to the overall cluster orientations). We therefore assign nodal planes strikes with a normal distribution with a mean of 30^o and a standard deviation of 5^o, dips with a normal distribution with a mean of 90^o and a standard deviation of 5^o, and rakes with a normal distribution with a mean of 180^o and a standard deviation of 5^o. Stress drops are assigned with a uniform distribution ranging from 0.1 $< \Delta\sigma <$ 10 MPa, from which the rupture dimensions and displacement are computed using the event magnitude. We assume a Young's moduli of 50 GPa and a Poisson's ratio of 0.25, based on values for the Duvernay observed by Soltanzadeh et al. (2015) and Weir et al. (2017).

To determine the impact on the NS1 fault, we resolve the modelled stress changes into shear and normal stresses acting on a vertical, right-lateral strike-slip fault with a strike of 5^o. The results of our stress modelling – the changes in the Mohr-Coulomb criteria (Equation 2) – are plotted in Figure 9. We observe that the modelled stress changes are small, less than 0.01 MPa at the point where the first events on the NS1 fault are observed. Moreover, the events on NS1 lie within a lobe of negative CFS change, indicating that the stress changes move the NS1 feature away from, rather than towards, failure.

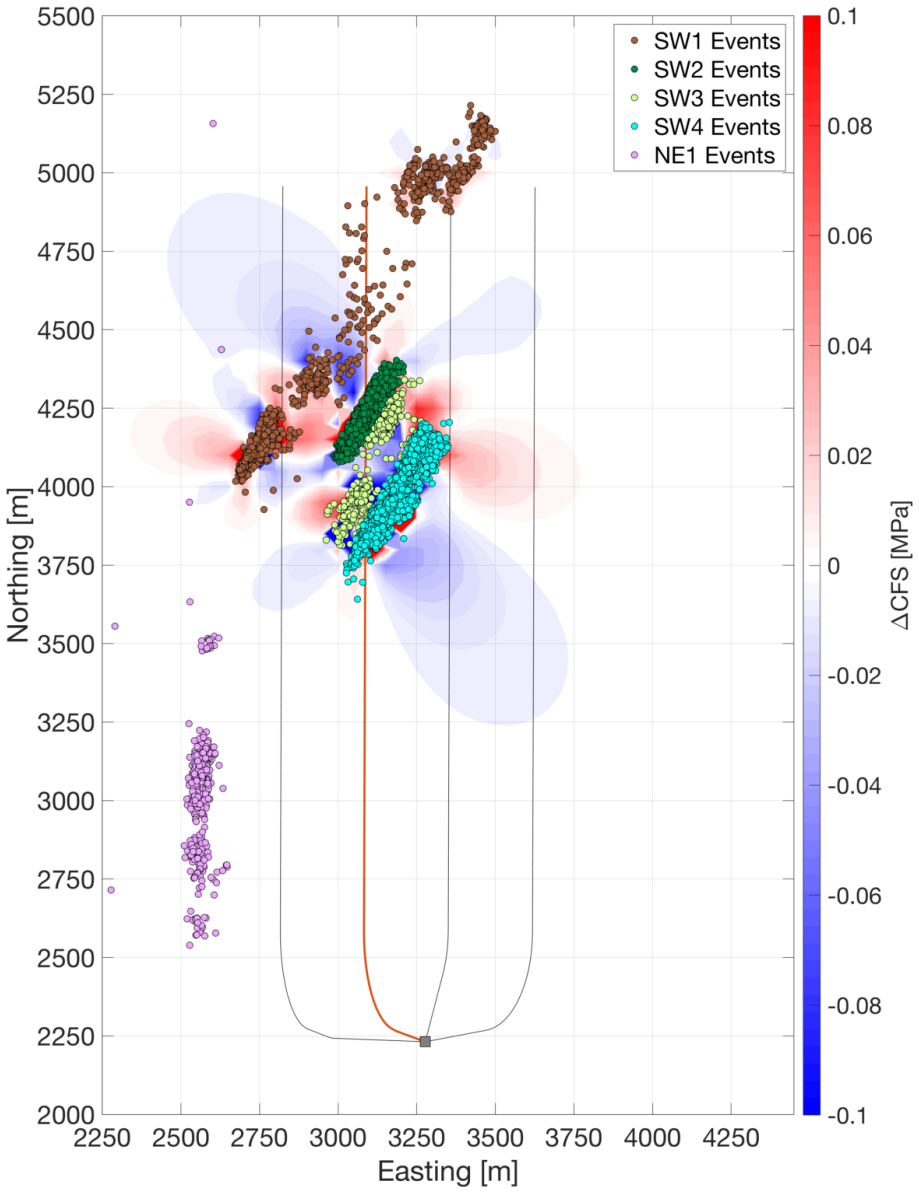

Figure 9: Changes in Mohr-Coulomb failure criteria (ΔCFS) produced by the slip of the events in the SW clusters, resolved onto the NS1 fault orientation. Here we show the cumulative stress change produced by all of the clusters. The impacts on the NS1 fault events (pink) are small, and actually lie within a lobe of negative ΔCFS.

The comparison between the modelled pore fluid pressure changes and the modelled stress transfer produces a clear conclusion. Our fluid flow models suggest an increase in pore pressure of approximately 0.5 MPa at the fault, which would decrease the effective normal stress acting on the fault, pushing it towards failure. In contrast, the stress transfer modelling produces a negative CFS change of less than 0.01 MPa. Therefore, it is clear the observed seismicity on the NS1 fault is driven by pore pressure transfer via a hydraulic connection, rather than by stress transfer between events transmitted through the rock frame.

662 **4.3 Implications for risk assessment**

663 There are several observations from this dataset that are useful for risk assessment of hydraulic
664 fracturing. We first consider the idea of risk assessment through analysis of reflection seismic
665 data and then move toward real-time approaches and give examples from the literature.

666 Eaton et al. (2018) examined the 3D/3C reflection seismic data at this site. They were able to
667 identify faults, but found that there was limited evidence for spatial correlation between faults
668 imaged by the reflection seismic and features reactivated by the seismicity. For example, the
669 NS1 fault on which the largest events occurred was not expressed in the reflection seismic data,
670 whereas large faults near to the wells imaged by the reflection seismic (e.g., F2 and F6 of Eaton
671 et al., 2018) showed no signs of reactivation. This implies that we cannot rely on pre-drill site
672 selection using only the geometrical fault distance (e.g., Westwood et al., 2017) to mitigate
673 induced seismicity, because faults that are imaged may not reactivate, while seismic events may
674 occur on faults that were not imaged.

675 Since we cannot directly image all faults in the subsurface, we assume that critically-stressed
676 faults may be distributed throughout a given volume of rock. If this is the case, then the
677 probability that a given industrial activity triggers seismicity will depend on the size of the rock
678 volume that it perturbs. In low permeability, intact shale rocks, the volume of rock affected by
679 hydraulic fracturing will be relatively small, and therefore the probability of intersecting a
680 critically-stressed fault would be low. However, in this study we show that the presence of pre-
681 existing permeable fracture networks may significantly increase the volume of rock that is
682 affected by the hydraulic fracturing, and therefore will increase the probability of causing
683 induced seismicity. A similar case has been observed in the Exshaw Formation in Alberta,
684 Canada, where Galloway et al. (2018) suggest that karst collapse along near-vertical faults
685 served as a conduit for vertical pressure transfer.

686 Various methods can be used to image subsurface fracture networks. For example, aligned
687 fractures will create seismic anisotropy that can be imaged by seismic reflection surveys (e.g.,
688 Hall and Kendall, 2003). Once wells have been drilled, fracture networks may be imaged by
689 borehole imaging logs. Geomechanical reconstructions can also be used to simulate the
690 expected fracture networks (e.g., Bond et al., 2013). However, as mentioned above we cannot
691 be sure that such methods will positively identify faults and fracture networks that may be of
692 concern.

693 Therefore, our study suggests that a proactive approach to mitigating seismicity is required,
694 where high-quality real-time microseismic monitoring is used to identify and map subsurface

structures that are being perturbed by the stimulation. This type of approach, in conjunction with the use of a traffic light protocol (TLP), would be ideal. A TLP is a risk mitigation approach that outlines a series of steps that are to be taken if events of certain magnitudes are observed (Atkinson et al., 2020). Most TLPs have a 'red light' condition where the operator would stop injection for a period of time and shut-in the well, and there are also intermediate steps such as reducing injection rates.

Through real-time monitoring, if an operator is able to image and understand the geomechanical impacts of their activities on adjacent faults and fracture networks, then it is possible to re-design hydraulic fracturing programs such that the likelihood of causing large events is reduced (e.g., Clarke et al., 2019; Kwiatek et al., 2019). This can be done, for example, by skipping stages within wells, by adjusting pumping parameters, or by changing the properties of the injected fluids. Successful examples of this kind of mitigation can be found in the literature for both hydraulic fracturing and enhanced geothermal stimulation. For example, Rich et al. (2019) details a case of hydraulic fracturing an 8-well pad that experienced induced seismicity with magnitudes up to ML 3.5. During the stimulation of the first few wells, using a 25,000 surface geophone array, a TLP, and real-time monitoring, the authors were able to identify lineations along which seismicity was travelling distances of up to 3 km away. In subsequent wells, multiple stages were skipped that directly intersected the mapped features and the type of injection fluid was changed from slickwater to gel. The result of this was a significant decrease in induced seismicity from the subsequent wells. Another successful example is from an enhanced geothermal project in Finland (Kwiatek et al., 2019). The authors used real-time monitoring to track the relationship between cumulative injected volume and the cumulative energy released by the observed seismic events. By identifying changes in the rate of seismicity relative to the injection volume, they were able to successfully modify their injection schedule and did not trigger any events over magnitude 2.1.

The key to mitigation in regions with a heightened risk of induced seismicity is real-time monitoring with a sophisticated monitoring system. As more detailed studies of fault activation due to hydraulic fracturing are carried out, improved methods for assessing, mitigating, and responding to induced seismicity will be developed, and the importance of a pre-existing fracture network should not be overlooked.

5. CONCLUSIONS

Hydraulic fracturing induced seismicity reflects a complex interplay between different mechanisms of stress transfer and the conditions in the subsurface. For this dataset, we show that hydraulic fracturing resulted in operationally induced seismicity, the activation of pre-

existing fracture networks and the activation of faults. Reactivation of a fault adjacent to the wells, with a strike length of at least 1.5 km, was likely initiated by transfer of fluid pressure along pre-existing fracture networks, resulting in activation over 1 km away from injection. These fractures allowed the pressure pulse to propagate much further from the well than would be expected if the low-permeability shale rock were otherwise intact. Seismic anisotropy was shown to be a potentially useful tool in imaging fracture networks, with anisotropy close to the wells aligning with the observed 30˚ fracture networks.

Modelling of the fluid flow along the fracture networks demonstrates the ability of the fracture networks to transmit sufficient changes in pore pressure to the fault at the observed distances. By matching the timing of the observed seismicity along the fault to the pore pressure increase, an approximate permeability is obtained that falls within an order of magnitude of permeability values from laboratory results. An observational argument allowed for the exclusion of poroelastic effects as a dominant force to explain our observations, and modelling of the Coulomb stress change showed that the events themselves produce insufficient stress change to trigger activity along the fault.

The approach used in this paper can be used to aid in the mitigation and interpretation of other cases of hydraulic fracturing induced seismicity. The steps taken to differentiate types of seismicity in this dataset may be applied to other datasets, and the methods can be adapted to real-time monitoring. A pro-active approach with a traffic light system and flexibility with the stimulation program are key to mitigating induced seismicity in areas of suspected permeable fracture networks.

Acknowledgements

The ToC2ME program was enabled by generous support from two companies. Continuous raw data (geophone and broadband recordings, network code TC2ME) are available through the IRIS Data Center following a holdback period that expires on July 1, 2020. The seismicity catalog used to prepare the figures in this manuscript is provided as a Supplementary data table. Financial support was provided by Chevron and the Natural Sciences and Engineering Research Council of Canada (NSERC) through the NSERC-Chevron Industrial Research Chair in Microseismic System Dynamics. James Verdon's contribution to this study was funded by the Natural Environment Research Council (NERC) under the UK Unconventional Hydrocarbons Project, Challenge 2 (Grant No. NE/R018162/1). Continuous geophone data were recorded under license from Microseismic Inc. for use of the BuriedArray method. TGS is sincerely thanked for providing the 3D multicomponent seismic data used in this analysis. CGG and Seisware are thanked for providing GeoSoftware used to display and interpret the seismic data.

All sponsors of the Microseismic Industry Consortium are also sincerely thanked for their ongoing support. Nadine Igonin was supported through the NSERC PGS-D, the SEG Reba C. Griffin Memorial Scholarship, and this collaboration was funded through the NSERC MSFSS. We thank Emerson Automation Solutions for the use of their Tempest reservoir modelling tools, and specifically Paul Childs for his helpful discussions as to the application of this software.

References

Atkinson, G.M., D.W. Eaton, H. Ghofrani, D. Walker, B. Cheadle, R. Schultz, R. Shcherbakov, K. Tiampo, J. Gu, R.M. Harrington, Y. Liu, M. van der Baan, H. Kao, 2016. Hydraulic fracturing and seismicity in the Western Canada Sedimentary Basin: Seismological Research Letters 87, 631-647.

Atkinson, G.M., D.W. Eaton, and N. Igonin., 2020, Developments in understanding seismicity triggered by hydraulic fracturing: Nature Reviews, Volume 1, p1-14., https://doi.org/10.1038/s43017-020-0049-7.

Bao X. and D.W. Eaton, 2016. Fault activation by hydraulic fracturing in Western Canada: Science 354, 1406-1409.

Batzle M. and Z. Wang, 1992. Seismic properties of pore fluids: Geophysics 57, 1396-1408.

Bond C.E., R. Wightman, P.S. Ringrose, 2013. The influence of fracture anisotropy on CO_2 flow: Geophysical Research Letters 40, 1284-1289.

Brace W.F., 1980. Permeability of crystalline and argillaceous rocks: International Journal of Rock Mechanics, Mining Science and Geomechanics 17, 241-251.

Caffagni E., D.W. Eaton, J.P. Jones, M. Van der Baan, 2016. Detection and analysis of microseismic events using a Matched Filtering Algorithm (MFA): Geophysical Journal International 206, 644-658.

Clarke H., L. Eisner, P. Styles, P. Turner, 2014. Felt seismicity associated with shale gas hydraulic fracturing: The first documented example in Europe: Geophysical Research Letters 41, 8308-8314.

Clarke H., J.P. Verdon, T. Kettlety, A.F. Baird, J-M. Kendall, 2019. Real time imaging, forecasting and management of human-induced seismicity at Preston New Road, Lancashire, England: Seismological Research Letters 90, 1902-1915

Darold A., A.A. Holland, C. Chen, A. Youngblood, 2014. Preliminary analysis of seismicity near Eagleton 1-29, Carter County, July 2014: Oklahoma Geological Survey Open-File Report OF2-2014.

Deng K., Y. Liu, R.M. Harrington, 2016. Poroelastic stress triggering of the December 2013 Crooked Lake, Alberta, induced seismicity sequence: Geophysical Research Letters 43, 8482-8491.

Dunn L., G. Schmidt, K. Hammermaster, M. Brown, R. Bernard, E. Wen, R. Befus, S. Gardiner, 2012. The Duvernay Formation (Devonian): Sedimentology and reservoir characterization of a shale gas/liquids play in Alberta, Canada: GeoConvention, Calgary, Article 90174.

Eaton, D.W., 2018. Passive seismic monitoring of induced seismicity: fundamental principles and application to energy technologies. Cambridge University Press.

Eaton D.W., N. Igonin, A. Poulin, R. Weir, H. Zhang, S. Pellegrino, G. Rodriguez, 2018. Induced seismicity characterisation during hydraulic fracture monitoring with a shallow-

wellbore geophone array and broadband sensors: Seismological Research Letters 89, 1641-1651.

Ekpo E., D. Eaton, R. Weir, 2017. Basement Tectonics and Fault Reactivation in Alberta Based on Seismic and Potential Field Data. In Okiweli A. (ed.), Geophysics. Intechopen, London.

Ekpo, E., 2020. Geophysical constraints on basement faulting in west-central Alberta: Implications for induced seismicity and post-collisional modification of western Laurentia. PhD Thesis, University of Calgary, Calgary, Canada.

Ellsworth, W. L., 2013. Injection-induced earthquakes: Science 341, 1225942-1:7.

Emerson 2014. Tempest Reservoir Engineering: accessed at: http://www.emerson.com/documents/automation/tempest-more-data-sheet-2014-en-82050.pdf on 03.08.2018.

Eyre, T.S., D.W. Eaton, D.I. Garagash, M. Zecevic, M. Venieri, R. Weir, D.C. Lawton, 2019a. The role of aseismic slip in hydraulic fracturing-induced seismicity: Science Advances 5, eaav7172.

Eyre, T.S., D.W. Eaton, M. Zecevic, D. D'Amico, D. Kolos, 2019b. Microseismicity reveals fault activation before M_W 4.1 hydraulic-fracturing induced earthquake: Geophysical Journal International 218, 534-546.

Friberg P.A., G.M. Besana-Ostman, I. Dricker, 2014. Characterisation of an earthquake sequence triggered by hydraulic fracturing in Harrison County, Ohio: Seismological Research Letters 85, 1295-1307.

Galloway, E., Hauck, T., Corlett, H., Pană, D. and Schultz, R., 2018. Faults and associated karst collapse suggest conduits for fluid flow that influence hydraulic fracturing-induced seismicity. Proceedings of the National Academy of Sciences, 115(43), pp.E10003-E10012.

Ghanizadeh A., Bhowmik S., Haeri-Ardakani O., Sanei H., and Clarkson C., 2015a. A comparison of shale permeability coefficients derived using multiple non-steady-state measurement techniques: Examples from the Duvernay Formation, Alberta (Canada): Fuel, 140, 371-387.

Ghanizadeh A., Clarkson C., Aquino S., Ardakani O.H., and Sanei H., 2015b. Petrophysical and geomechanical characteristics of Canadian tight oil and liquid-rich gas reservoirs: I. Pore network and permeability characterization: Fuel, 153, 664-681.

Gischig, V., Doetsch, J., Maurer, H., Krietsch, H., Amann, F., Evans, K.F., Nejati, M., Jalai, R., Valley, B., Obermann, A., Weimer, S., and Giardini, D., 2018. On the link between stress field and small-scale hydraulic fracture growth in anisotropic rock derived from microseismicity: Solid Earth, 9(1), 36-61.

Green C.A., P. Styles, B.J. Baptie, 2012. Preese Hall shale gas fracturing review and recommendations for induced seismic mitigation. Department of Energy and Climate Change, London.

Goebel, T.H.W., Weingarten, M., Chen, X., Haffener, J. and Brodsky, E.E., 2017. The 2016 Mw5. 1 Fairview, Oklahoma earthquakes: Evidence for long-range poroelastic triggering at > 40 km from fluid disposal wells. Earth and Planetary Science Letters, 472, pp.50-61.

Gutenberg B., and C.F. Richter, 1944. Frequency of earthquakes in California: Bulletin of the Seismological Society of America 34, 185-188.

Hall S.A. and J-M. Kendall, 2003. Fracture characterization at Valhall: Application of P-wave amplitude variation with offset and azimuth (AVOA) analysis to a 3D ocean-bottom data set: Geophysics 68, 1150-1160.

Heidbach, O., M. Rajabi, K. Reiter, M. Ziegler and WSM Team, 2016. World stress map database release 2016, GFZ Data Services.

Holland A.A., 2013. Earthquakes triggered by hydraulic fracturing in south-central Oklahoma: Bulletin of the Seismological Society of America 103, 1784-1792.

Hosseini, B., and D.W Eaton, 2018, Fluid flow and thermal modeling for tracking induced seismicity near the Graham disposal well, British Columbia, Canada: SEG International Exposition and Annual Meeting, 14-19 October, Anaheim, California, USA.

Huang, L., & Liu, C. Y. 2017. Three Types of Flower Structures in a Divergent-Wrench Fault Zone. Journal of Geophysical Research: Solid Earth, 122(12), 10-478.

Igonin N., M. Zecevic, D.W. Eaton, 2018. Bilinear magnitude-frequency distributions and characteristic earthquakes during hydraulic fracturing: Geophysical Research Letters 45, 12866-12874.

Kao H., R. Visser, B. Smith, S. Venables, 2018. Performance assessment of the induced seismicity traffic light protocol for northeastern British Columbia and western Alberta: The Leading Edge 37, 117-126.

Kendall J-M. A. Butcher, A.L. Stork, J.P. Verdon, R. Luckett, B.J. Baptie, 2019. How big is a small earthquake? Challenges in determining microseismic magnitudes: First Break 37, 51-56

Keranen K.M., M. Weingarten, G.A. Abers, B.A. Bekins, S. Ge, 2014. Sharp increase in central Oklahoma seismicity since 2008 induced by massive wastewater injection: Science 345, 448-451.

Kettlety T., J.P. Verdon, M.J. Werner, J-M. Kendall, J. Budge, 2019. Investigating the role of elastostatic stress transfer during hydraulic fracturing-induced fault reactivation: Geophysical Journal International 217, 1200-1216.

Knapp, L., McMillan, J., and Harris, N., 2017. A depositional model for organic-rich Duvernay Formation mudstones, Sedimentary Geology, 347, 160-182.

Kozłowska, M., Brudzinski, M.R., Friberg, P., Skoumal, R.J., Baxter, N.D. and Currie, B.S., 2018. Maturity of nearby faults influences seismic hazard from hydraulic fracturing. Proceedings of the National Academy of Sciences, 115(8), pp.E1720-E1729.

Kwiatek, G. et al. Controlling fluid-induced seismicity during a 6.1-km-deep geothermal stimulation in Finland. Sci. Adv. 5, .eaav7224 (2019).

Lei, X., Wang, Z. & Su, J, 2019. The December 2018 ML 5.7 and January 2019 ML 5.3 earthquakes in South Sichuan Basin induced by shale gas hydraulic fracturing. Seismol. Res. Lett. 90, 1099–1110.

Lyster S., H.J. Corlett, H. Berhane, 2017. Hydrocarbon resource potential of the Duverney Formation in Alberta – Update: Alberta Energy Regulator/Alberta Geological Survey Open File Report 2017-02.

Maghsoudi, S., J. Baro, A. Kent, D.W. Eaton, J. Davidsen, 2018. Interevent Triggering in Microseismicity Induced by Hydraulic Fracturing: Bulletin of the Seismological Society of America, 108(3A), 1133-1146.

Maxwell S.C., J. Shemeta, E. Campbell, D. Quirk, 2008. Microseismic deformation rate monitoring: SPE Annual Technical Conference, Denver, SPE116596.

Maxwell, S.C., Jones, M., Parker, R., Leaney, S., Mack, M., Dorvall, D., D'Amico, D., Logel, J., Anderson, E. and Hammermaster, K., 2010. Fault activation during hydraulic fracturing. In 72nd EAGE Conference and Exhibition incorporating SPE EUROPEC 2010 (pp. cp-161). European Association of Geoscientists & Engineers.

Michael A.J., 1984. Determination of stress from slip data: faults and folds: Journal of Geophysical Research 89, 11517-11526.

899 Peacock, D.C.P., Nixon, C.W., Rotevatn, A., Sanderson, D.J., and Zuluaga, L.F., 2016.
900 Glossary of fault and other fracture networks, Journal of Structural Geology, 92, 12-29.

901 Pennington C. and X. Chen, 2017. Coulomb stress interactions during the M_W 5.8 Pawnee
902 sequence: Seismological Research Letters 88, 1024-1031.

903 Poulin, A. et al. 2019, Focal-time analysis: A new method for stratigraphic depth control of
904 microseismicity and induced seismic events. Geophysics 84, KS173– KS182.

905 Questiaux, J-M., Couples, G., and Ruby, N., 2010. Fractured reservoirs with fracture corridors,
906 Geophysical Prospecting, 58(2), 279-295.

907 Rich, J., Bailey, A., Jreij, S. & Klepacki, D. High- resolution insights into hydraulic fracturing
908 strike-slip seismicity: hypocenter uncertainty, depth of initiation, and genesis mechanisms.
909 In SEG Technical Program. Expanded Abstracts 2019 3046-3050 (Society of Exploration
910 Geophysicists, 2019).

911 Rodroguez, G., and D.W. Eaton, 2020. Ground-Motion Analysis of Hydraulic-Fracturing
912 Induced Seismicity at Close Epicentral Distance, Bulletin of the Seismological Society of
913 America, 110(1), 331-344.

914 Rogers, S. F., 2003. Critical stress-related permeability in fractured rocks. Geological Society,
915 London, Special Publications, 209(1), 7-16.

916 Schoenball M., F. R. Walsh, M. Weingarten, W.L. Ellsworth, 2018. How faults wake up: the
917 Guthrie-Langston, Oklahoma earthquakes: The Leading Edge 37, 100-106.

918 Schultz R., V. Stern, M. Novakovic, G. Atkinson, Y.J. Gu, 2015a. Hydraulic fracturing and the
919 Crooked Lake sequences: Insights gleaned from regional seismic networks: Geophysical
920 Research Letters 42, 2750-2758.

921 Schultz R., S. Mei, D. Pana, V. Stern, Y. J. Gu, A. Kim, D. Eaton, 2015b. The Cardston
922 earthquake swarm and hydraulic fracturing of the Exshaw Formation (Alberta Bakken play):
923 Bulletin of the Seismological Society of America 105, 2871-2884.

924 Schultz R., R. Wang, Y.J. Gu, K. Haug, G. Atkinson, 2017. A seismological overview of the
925 induced earthquakes in the Duvernay play near Fox Creek, Alberta: Journal of Geophysical
926 Research 112, 492-505.

927 Segall, P. and Lu, S., 2015. Injection-induced seismicity: Poroelastic and earthquake nucleation
928 effects. Journal of Geophysical Research: Solid Earth, 120(7), pp.5082-5103.

929 Shapiro S., and Dinske C., 2009. Fluid-injection seismicity: pressure diffusion and hydraulic
930 fracturing: Geophysical Prospecting, 57(2), 301-310.

931 Shipman, T., MacDonald, R. and Byrnes, T., 2018. Experiences and learnings from induced
932 seismicity regulation in Alberta. Interpretation, 6(2), pp.SE15-SE21.

933 Skoumal R.J., M.R. Brudzinski, B.S. Currie, 2015. Induced earth-quakes during hydraulic
934 fracturing in Poland Township, Ohio: Bulletin of the Seismological Society of America 105,
935 189-197.

936 Soltanzadeh M., Davies G., Fox A., Hume D., and Rahim N., 2015. Application of mechanical
937 and mineralogical rock properties to identify fracture fabrics in the Devonian Duvernay
938 formation in Alberta: Unconventional Resources Technology Conference, URTeC
939 2178289.

940 Stein R.S., G.C.P. King, J. Lin, 1992. Change in failure stress on the southern San Andreas
941 fault system caused by the 1992 magnitude = 7.4 Landers earthquake: Science 258, 1328-
942 1332.

943 Talwani P. and S. Acree, 1984. Pore pressure diffusion and the mechanism of reservoir-induced
944 seismicity: Pure and Applied Geophysics 122, 947-965.

Teanby N.A., J-M. Kendall, M. van der Baan, 2004. Automation of shear-wave splitting measurements using cluster analysis: Bulletin of the Seismological Society of America 94, 453-463.

van der Elst N.J., H.M. Savage, K.M. Keranen, G.A. Abers, 2013. Enhanced remote earthquake triggering at fluid-injection sites in the midwestern United States: Science 341, 164-167.

Verdon J.P., A. Wuestefeld, J.T. Rutledge, I.G. Main, J-M. Kendall, 2013. Correlation between spatial and magnitude distributions of microearthquakes during hydraulic fracture stimulation: 75th EAGE Conference, London, Expanded Abstracts Th-01-12.

Verdon J.P., A.L. Stork, R.C. Bissell, C.E. Bond, M.J. Werner, 2015. Simulation of seismic events induced by CO_2 injection at In Salah, Algeria: Earth and Planetary Science Letters 426, 118-129.

Verdon J.P., J-M. Kendall, S.P. Hicks, P. Hill, 2017. Using beamforming to maximise the detection capability of small, sparse seismometer arrays deployed to monitor oil field activities: Geophysical Prospecting 65, 1582-1596.

Viegas G., T. Urbancic, and H. Chittenden, 2018. Influence of geological setting on stress released by hydraulic fracture-induced earthquakes: First Break 36, 77-81.

Wang, R., Lorenzo Martín, F., Roth, F., 2006: PSGRN/PSCMP - a new code for calculating co- and post-seismic deformation, geoid and gravity changes based on the viscoelastic-gravitational dislocation theory, Computers and Geosciences, 32, 4, 527-541.

Wang R., Y.J. Gu, R. Schultz, A. Kim, G. Atkinson, 2016. Source analysis of a potential hydraulic-fracturing-induced earthquake near Fox Creek, Alberta: Geophysical Research Letters 43, 564-573.

Wang, R., Gu, Y. J., Schultz, R., & Chen, Y., 2018. Faults and non-double-couple components for induced earthquakes. Geophysical Research Letters, 45(17), 8966-8975.

Weir R., Eaton D., Lines L., Lawton D., and Ekpo E., 2017. Inversion and interpretation of seismic-derived rock properties in the Duvernay play: Interpretation, 6(2), SE1-SE14.

Westaway R., 2017. Integrating induced seismicity with rock mechanics: a conceptual model for the 2011 Preese Hall fracture development and induced seismicity: In E.H. Rutter, J. Mecklenburgh, K.G. Taylor (eds) *Properties of Mudrocks*, Geological Society of London Special Publications 454, 327-359.

Westwood R.F., Toon S.M., Styles P., Cassidy N.J., 2017. Horizontal respect distance for hydraulic fracturing in the vicinity of existing faults in deep geological reservoirs: a review and modelling study: Geomechanics and Geophysics for Geo-Energy and Geo-Resources 3, 379-391.

Wilson M.P., Worrall F., Davies R.J., Almond S., 2018. Fracking: How far from faults?: Geomechanics, Geophysics and Geophysics for Geo-Energy and Geo-Resources 4, 193-199.

Zhang H., D.W. Eaton, G. Rodriguez, S.Q. Jia, 2019. Source-mechanism analysis and stress inversion for hydraulic-fracturing-induced event sequences near Fox Creek, Alberta: Bulletin of the Seismological Society of America, in press.

Zhang, H., D. W. Eaton, G. Li, Y. Liu, and R. M. Harrington, 2016. Discriminating induced seismicity from natural earthquakes using moment tensors and source spectra, J. Geophys. Res. Solid Earth, 121, 972–993, doi:10.1002/2015JB012603.

SUPPLEMENTARY MATERIAL

The supplementary material includes a discussion on the depths of the events and the model parameters for pore pressure modelling.

Additionally, the following external files are included with the submission:

- Catalog of events
- Video of event occurrence over time
- Video of pore pressure perturbation over time

Event depths

A north-south cross section showing the event depth distribution is shown in Figure S1. The hypocentre locations were determined as follows:

1. Initial locations were obtained by beam-forming with a short-time average/long-time average method (Verdon et al, 2017) using a velocity model derived from P- and S-wave sonic logs (Eaton et al., 2018).
2. Based on these locations, the corresponding P- and S-wave picks were computed by forward modelling.
3. The focal-time method (Poulin et al., 2019) was used to recalculate event depths, from which the stratigraphic level can be inferred based on well ties (Weir et al., 2017).

In more detail, the beam-forming approach provides hypocenter coordinates (*x,y,z,t*) corresponding to the point in that 4D space where the beamformed STA/LTA stack is maximized. The forward modelling to compute the corresponding P- and S-wave picks used an eikonal solver (Verdon et al., 2017), with the same velocity model as in step 1. The focal-time method requires correlation of equivalent P-P and P-S reflections, using 3-D multicomponent seismic data. The time difference between the corresponding reflections is equivalent to the S-P time for a microseismic event, extrapolated to zero offset (Poulin et al., 2019). This approach does not require an explicit velocity model for event location, since the underlying velocity information (including anisotropy) is implicit in the P-P and P-S reflection correlation; rather, this approach provides a direct lookup table to convert S-P time at zero offset with P-wave time in the 3-D seismic section. Time-depth relationships obtained from seismic well ties can then be used for robust determination of the stratigraphic depth level of the event. In this case, the lookup table for the ToC2ME dataset, developed by Poulin et al. (2019), was available for determining focal depths of events.

As shown in Figure S-1, the vast majority of the events are located at or above the depth of the wellbore, including most of the largest events. Though there is some evidence for downward growth into the basement, most of the induced seismicity occurred in the Ireton Formation. Therefore, both the fracture network and activated portion of the faults appear to be limited stratigraphically.

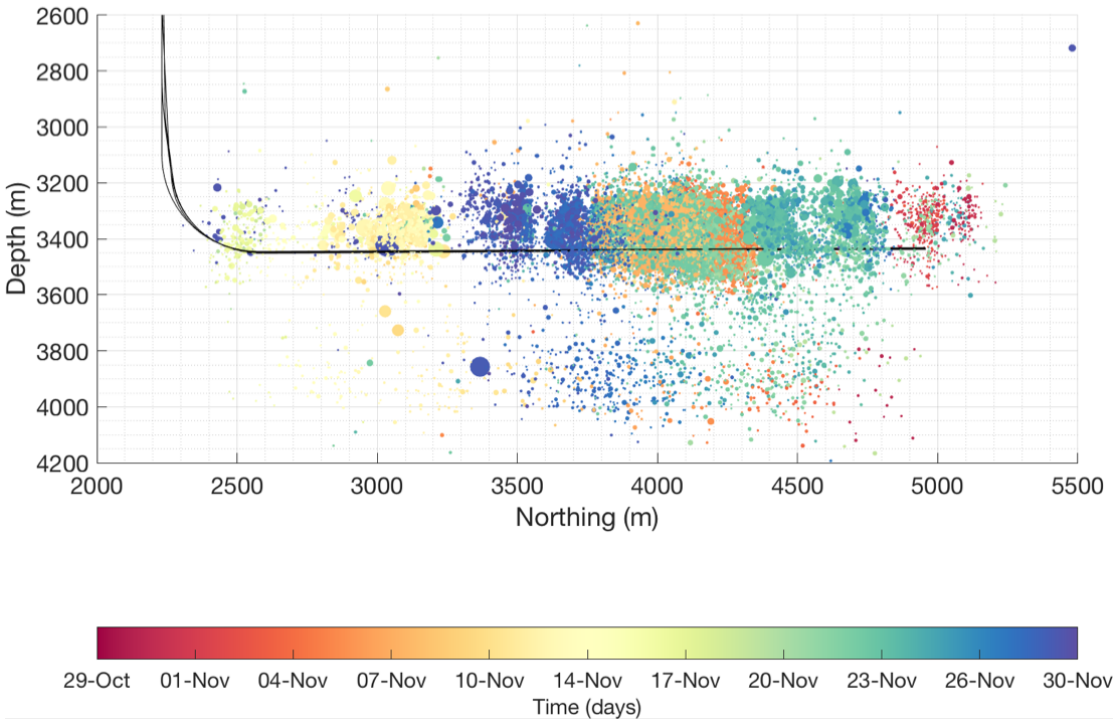

Figure S1: Depth distribution over time. Black lines are the well trajectories, and events are coloured in time, and scaled by size.

Pore pressure model parameters

The parameterization of the pore-pressure modelling is documented in the attached file FractureSimulation.dat. This is an input file for Emerson's Tempest software (Emerson, 2014). The file is keyword-driven: comments in the file detail what parameters are defined by each keyword.